Towards Quantitative Evaluation of Wall Shear Stress from 4D Flow Imaging

Sébastien Levilly, Marco Castagna, Jérôme Idier, Félicien Bonnefoy, David Le Touzé, Perrine Paul-Gilloteaux, Saïd Moussaoui, Jean Michel Serfaty

To cite this version:

Sébastien Levilly, Marco Castagna, Jérôme Idier, Félicien Bonnefoy, David Le Touzé, et al.. Towards Quantitative Evaluation of Wall Shear Stress from 4D Flow Imaging. Magnetic Resonance Imaging, 2020, 10.1016/j.mri.2020.08.017 . hal-02564861

HAL Id: hal-02564861
https://hal.science/hal-02564861v1

Submitted on 6 Nov 2020

Towards Quantitative Evaluation of Wall Shear Stress from 4D Flow Imaging

Sébastien Levilly[a,*], Marco Castagna[b,c], Jérôme Idier[a], Félicien Bonnefoy[b], David Le Touzé[b], Perrine Paul-Gilloteaux[c], Saïd Moussaoui[a], Jean-Michel Serfaty[c]

[a] *Laboratoire des Sciences du Numérique de Nantes, 1 rue de la Noë, BP 92101, 44321 Nantes Cedex 3, France*
[b] *Ecole Centrale de Nantes, LHEEA Lab (ECN and CNRS), 1 rue de la Noë, 44300 Nantes, France*
[c] *Université de Nantes, CHU Nantes, Inserm, SFR Santé, Inserm UMS 016, CNRS UMS 3556, F-44000 Nantes*

Abstract

Wall shear stress (WSS) is a relevant hemodynamic indicator of the local stress applied on the endothelium surface. More specifically, its spatiotemporal distribution reveals crucial in the evolution of many pathologies such as aneurysm, stenosis, and atherosclerosis. This paper introduces a new solution, called PaLMA, to quantify the WSS from 4D Flow MRI data. It relies on a two-step local parametric model, to accurately describe the vessel wall and the velocity-vector field in the neighborhood of a given point of interest. Extensive validations have been performed on synthetic 4D Flow MRI data, including four datasets generated from patient specific computational fluid dynamics simulations on carotids. The validation tests are focused on the robustness with respect to noise and on the impact of the resolution level in the context of complex flow patterns. The WSS quantification performance reached by PaLMA is significantly higher than the reference one obtained using the smoothing B-spline method proposed by Potters *et al.* (2015) method, while the computation time is equivalent for both WSS quantification methods.

Keywords: Wall Shear Stress, 4D Flow MRI, Computational Fluid Dynamics (CFD), Carotid Bifurcation, Stenosis

---

Disclosure

Declaration of interest: none

1. Introduction

1.1. State of the Art

In the last decade, the hemodynamic conditions of blood flow have been the subject of intensive investigations in the context of cardiovascular diseases such as aneurysms [1], stenosis [2, 3], atherosclerosis [4] or bicuspid aortic valve affliction [5]. It is currently admitted that complex

---

[*] Corresponding author
Email address: `levilly.sebastien@gmail.com` (Sébastien Levilly)

hemodynamic conditions play an important role in the evolution of such pathologies. In this regard, the Wall Shear Stress (WSS) is a promising hemodynamic parameter, since it characterizes the local stress applied on the endothelium surface. Specifically, [4, 6] have shown the effect of WSS on the organization of the endothelial cells. The impact of WSS has been studied on several cardiovascular pathologies, in terms of magnitude [1, 7], of axial and circumferential direction [8], and of time variation using the Oscillatory Shear Index (OSI) [9, 10].

In order to assess the WSS at a given point of the vessel wall, a prerequisite step is to evaluate the spatial velocity derivatives at this point. 4D Flow MRI is a phase-contrast (PC) MRI sequence that quantifies the blood flow as velocity vectors over time, with full volumetric coverage[1]. Unfortunately, near-wall values of velocity magnitude being small, the effect of the acquisition noise and of limited spatial resolution strongly degrades the evaluation precision of such spatial derivatives [1, 12]. Under clinical acquisition constraints, 4D Flow MRI data has a voxel resolution limited to 1-1.2 mm ISO for intracranial, and to 2-2.5 mm ISO for thoracic acquisitions [14]. As regards the velocity noise, its standard deviation is about 5 % of the velocity encoding (Venc) based on anatomic signal-to-noise-ratio (SNR) in thoracic measurements with a 1.5T MRI and no contrast enhancement [15]. In such conditions, it remains a challenging issue to compute WSS values with a truly quantitative meaning, and this has motivated continued efforts to produce improved WSS estimation methods along distinct strategies [5, 12, 16, 17].

Table 1 presents a selected set of existing methods, with a distinction between local methods and global ones, and whether the methods are regularized or not. Global methods [12, 18, 16, 13, 2, 3] evaluate the WSS at all the segmented points of the wall simultaneously, while the local ones focus at given points of interest (POI) [5, 17, 11, 19]. In this regard, local methods can be considered as more flexible, since the radiologist is free to restrict the computation of WSS values within ROIs of specific clinical interest.

	No regularization	Regularized methods
Local design	Cylindrical frame [5]	Sectorial parabolic model [11] Parabolic model [19] Smoothing B-spline [17] ([20, 7, 10, 21])
Global design	B-spline [12] ([9, 6]) Finite difference [18]	5th Order polynomial [16] Finite-element model [13, 2] ([8]) Sobel filter [3]

Table 1: Selected set of existing WSS evaluation methods. Related WSS studies are in brackets.

On the other hand, regularization is a general principle that aims at incorporating additional structural information to counterbalance the unstable character of inverse problem solutions [22]. In the context of WSS estimation from 4D Flow MRI data, regularization can take the form of a constraint, *e.g.,* the nullity constraint of the velocity at the vessel wall [11, 19, 17, 2], possibly combined with a parametric model [16, 19]. In [17], the nullity constraint is considered at the POI only, while in [11, 2], it is imposed on a circular arc and on the whole segmented vessel

---

[1] By contrast, 2D time-resolved PC MRI is limited to 2D slice acquisitions [11, 12, 5, 13].

wall, respectively. Regularized methods generally yield solutions that are more robust to noise, but with the risk of underestimating the quantity of interest, *i.e.*, of introducing a significant level of bias while reducing the variance in the case of complex velocity fields. This explains why methods such as those proposed in [17, 3] tend to provide WSS values with underestimated levels and variations, both spatially and temporally [10]. Yet, regularized methods may still reach fairly high correlation values between the estimated WSS and the true one. For instance, a coefficient of determination $r^2 = 71\,\%$ (*i.e.*, a Pearson correlation index $r = 84\,\%$) is reported in [21], which clearly indicates that such a regularized WSS estimation method is operative. However, our contribution is motivated by the feeling that some margin of improvement is still possible within the local, model-based framework.

1.2. Contribution

Our goal is to propose a new local, regularized WSS estimation method, with enhanced performance, both in terms of absolute error and of correlation to the true WSS level. For that purpose, we rely on two parametric models under the form of low-order polynomials. The first one is a cubic surface model of the vessel wall, and the second one is a trivariate model of the velocity field, defined conditionally to the previous one. Both are defined at given POIs and at given times, by reference to the local behavior of the wall shape for the surface model and of the velocity field for the trivariate model, respectively.

Akin to previous contributions such as [19, 17], we deduce the value of the WSS at any considered POI from a locally estimated analytical model of the blood velocity field. Thanks to our volumetric modeling, we propose to perform a new robust *a posteriori* reestimation step, in order to exploit the fact that several estimated values of the WSS are available for each POI. Moreover, in contrast with existing local WSS estimation methods, our method fully exploits the volumic character of the available data at all of its steps. In comparison, Potters *et al.* [17] deduce the WSS value from a one-dimensional B-spline interpolation step. In this regard, our approach is closer to Sotelo *et al.*'s contribution [2], which is also fully 3D based, but using a global approach. In addition, our solution aims to model the velocity field in 3D, including the vessel shape input, in a design inspired from related work limited to 2D-based velocity model [11]. Another distinctive feature of our contribution is the explicit presence of a spatial filter in our model, accounting for the partial volume effect due to the limited resolution of 4D Flow MRI data.

Section 2 contains a detailed presentation of the proposed WSS quantification method, called *Parametric Local Morphology Algorithm* (PaLMA). Section 3 presents the simulated data and the performance indices that have been considered to evaluate the performance of PaLMA. Finally, Section 4 is dedicated to comparative results.

2. Parametric Local Morphology Algorithm (PaLMA)

2.1. Principle

PaLMA comprises four distinct steps, at each time instant (see Figure 1):

1. At a given POI, the shape of the vessel wall is first identified as a cubic surface model in the neighborhood of a POI, *i.e.*, for all vertex points belonging to a region of interest (ROI) centered around the POI.

2. Then, the 4D Flow MRI data points are processed in the same ROI, in order to estimate a continuous map of the blood velocity field inside the vessel, around the POI. A polynomial model is used for each component of the blood velocity field, for which the no-slip condition is enforced uniformly over the local surface.
3. WSS values at the POI and at all vertices in the ROI can be easily deduced by explicit analytical derivation from the estimated polynomial model of the blood velocity field.
4. Once the latter steps have been performed for a distributed set of POI, several distinct values are available for the WSS estimation at a given POI. A final robust estimation step is then performed to deduce a unique WSS value.

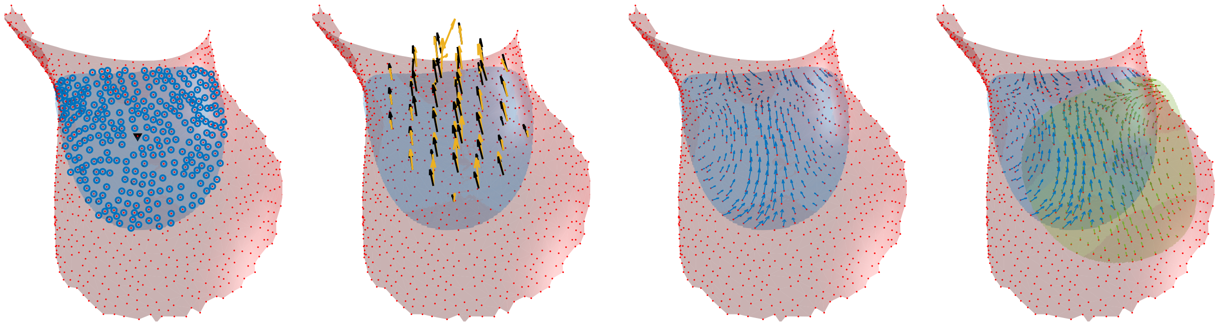
(a) Step 1 (b) Step 2 (c) Step 3 (d) Step 4

Figure 1: The four steps of PaLMA. (a) Fit a cubic surface (in blue) to the local vertices describing the segmented wall within the ROI. (b) Fit polynomial model (yellow arrows) to the 4D MRI datapoints (black arrows) in the ROI. (c) Deduce WSS vectors at each local vertex (blue arrows). (d) Distinct intersecting ROIs (*e.g.,* in blue and in green) provide distinct WSS estimation values at a given POI.

In the remaining parts of this section, we provide additional information about each step of PaLMA. In practice, PaLMA is a standalone Matlab code[2].

2.2. Step 1: Vessel Wall Model Fitting

A local Cartesian coordinate system $\mathcal{L}$ is defined for each segmentation point of the vessel wall such that the z-axis aligns with the inward normal vector $\vec{n}$. In order to optimally fit the surface model, we assume that vertices and faces describing the vessel wall are available from a segmentation step performed at an early stage. The normal vector $\vec{n}$ is computed from the faces close to the POI.

A parametric surface must be chosen as a local model of the vessel wall. The family of paraboloids (*i.e.*, of quadric surfaces) is a common choice to describe surfaces in a local way in the field of computer graphics [23, 24, 25]. Some examples of paraboloid surface models can be found in the context of cardiovascular medical imaging [26, 27]. In 4D Flow MRI, we conducted some tests to fit the vessel wall using quadric surfaces. We observed that the results were not always satisfying, because the vessel shape is sometimes too complex to be locally described

---

[2] PaLMA is freely available on request from the authors for research purposes.

as a paraboloid. Here, we propose to rely on the broader family of *centered cubic surfaces*, corresponding to the following model in the local coordinate system $\mathcal{L}$:

$$z = S(x, y; \boldsymbol{\theta}) = ax + by + cxy + dx^2 + ey^2 + fyx^2 + gxy^2 + hx^3 + iy^3 \tag{1}$$

where $\boldsymbol{\theta} = [a, b, c, d, e, f, g, h, i]^{\mathrm{t}}$ is a parameter vector corresponding to nine degrees of freedom ($^{\mathrm{t}}$ denotes matrix transposition). In comparison, paraboloid surfaces would be obtained as a five dimension family by cancelling the four last parameters. Let us remark that $S(0, 0; \boldsymbol{\theta}) = 0$, so that the POI belongs to S.

The local surface parameters are obtained in two steps:

- For each POI, we define a local ROI corresponding to a ball centered at the POI and of a given radius R. In practice, we found that tuning R to three times the grid resolution is a reasonable choice.
- We then consider the n_R vertices that belong to the ROI, and we estimate $\boldsymbol{\theta}$ by linear least squares (LS). More details can be found in Appendix A.

Such a procedure can be repeated for different points of interest on the vessel wall. Typically, we successively consider the N_{s} available segmentation points to generate N_{s} local surface models.

2.3. Step 2: Velocity Model Fitting

In a second step, a local model of the velocity field is fitted to to the 4D Flow MRI data points of the ROI. We rely on a trivariate polynomial model for each component of the velocity field. Let $\vec{p} = (x, y, z)$ in the local system $\mathcal{L}$. For any $\vec{p}$ located in the ROI, we propose a velocity field model that reads

$$\vec{v}(\vec{p}; \boldsymbol{\gamma}) = B^{+}(\vec{p}) \times \begin{bmatrix} P(x, y, B(\vec{p}); \boldsymbol{\gamma}_x) \\ P(x, y, B(\vec{p}); \boldsymbol{\gamma}_y) \\ P(x, y, B(\vec{p}); \boldsymbol{\gamma}_z) \end{bmatrix}, \tag{2}$$

where

- $B(\vec{p}) = z - S(x, y; \hat{\boldsymbol{\theta}})$ is the algebraic distance of $\vec{p}$ from the wall model (1), and $B^{+}(\vec{p}) = \max\{B(\vec{p}), 0\}$ is the positive part of $B(\vec{p})$;
- $P(\vec{p}; \boldsymbol{\gamma})$ is a trivariate quadratic polynomial, *i.e.*,

  $$P(\vec{p}; \boldsymbol{\eta}) = \sum_{\substack{i,j,k \\ i+j+k \leq 2}} \eta_{ijk} x^i j^j z^k, \tag{3}$$

  $\boldsymbol{\eta}$ being a column vector gathering the set of $N_P = 10$ parameters $\{\eta_{ijk}, i + j + k \leq 2\}$.

Let us stress that such a model of velocity cancels uniformly along (and outside) the model of the vessel wall, *i.e.*, the no-slip condition is locally fulfilled everywhere on the vessel wall. Moreover, we introduce the algebraic distance $B(\vec{p})$ as the third component of the quadratic polynomials P in (2) in order to favor blood flows progressing along the modelled wall surface.

In order to fit the velocity model (2), we adjust $3N_P = 30$ free scalar parameters corresponding to $\boldsymbol{\gamma} = (\boldsymbol{\gamma}_x^{\mathrm{t}}, \boldsymbol{\gamma}_y^{\mathrm{t}}, \boldsymbol{\gamma}_z^{\mathrm{t}})^{\mathrm{t}}$, given N_R measured velocities located within the ROI. Let $\vec{u}_i$ refers to the i-th measured velocity, at position $\vec{p}_i$, both $\vec{u}_i$ and $\vec{p}_i$ being expressed in the local system $\mathcal{L}$. We propose to estimate $\boldsymbol{\gamma}$ using a weighted linear least-squares approach:

$$\hat{\boldsymbol{\gamma}} = \underset{\boldsymbol{\gamma} \in \mathbb{R}^{3N_P}}{\arg\min} \sum_{i=1}^{N_R} w_i \|\vec{u}_i - (h \star \vec{v})(\vec{p}_i; \boldsymbol{\gamma})\|_2^2, \tag{4}$$

where $\|\cdot\|$ denotes the Euclidian norm, and w_i is a nonnegative function allowing to put more weight on data points that are closer to the vessel wall. Following [25], we define w_i as $w(B(\vec{p}_i), M(\vec{p}_i))$, with $M(\vec{p}_i)$ the transversal magnetization at position $\vec{p}_i$, and

$$w(t, m) = \begin{cases} m(1 - (t/R)^2)^4 & \text{if } t < R, \\ 0 & \text{otherwise.} \end{cases}$$

On the other hand, $h \star \cdot$ corresponds to the spatial convolution with a point spread function (PSF) h, which stands for the limited resolution of the MRI scanner. This stage of the model relates the 4D Flow MRI measurements to the underlying velocity field. In a more specific way, it allows us to take account of the partial volume effect near the vessel wall.

Appendix B provides additional details about the practical computation of $\hat{\boldsymbol{\gamma}}$.

2.4. Step 3: WSS Quantification

At any given point $\vec{p}_{\delta\Omega}$ of the wall surface $\delta\Omega$ (and at a given instant), let us first define the *viscous stress vector* as $\vec{\tau}_{\mathrm{v}} = \bar{\bar{\tau}}_{\mathrm{v}} \cdot \vec{n}$, where $\bar{\bar{\tau}}_{\mathrm{v}}$ is the second-order viscous stress tensor and $\vec{n}$ is the inward unit vector normal to the wall surface $\delta\Omega$. The WSS $\vec{\tau}$ is the component of the viscous stress vector that is tangent to $\delta\Omega$, *i.e.*,

$$\vec{\tau} = \vec{\tau}_{\mathrm{v}} - (\vec{\tau}_{\mathrm{v}} \cdot \vec{n})\vec{n} \tag{5}$$

(let us mention that the normal component of the viscous stress $\vec{\tau}_{\mathrm{v}} \cdot \vec{n}$ is most often negligible with respect to the shear stress component). Considering blood as Newtonian, *i.e.*, as an incompressible fluid, the viscous stress tensor reads $\bar{\bar{\tau}}_{\mathrm{v}} = 2\mu\, \bar{\bar{D}}$, with μ the dynamic viscosity of blood and $\dot{\bar{\bar{\varepsilon}}}$ the strain-rate tensor, which is function of spatial derivatives of the velocity vector $\vec{v}$ at the considered point. As a consequence,

$$\vec{\tau}_{\mathrm{v}} = 2\mu \bar{\bar{D}} \cdot \vec{n} = \mu \left(\bar{\bar{\nabla}} \vec{v} + (\bar{\bar{\nabla}} \vec{v})^{\mathrm{t}} \right) \cdot \vec{n} = \mu \begin{bmatrix} 2\frac{\partial v_x}{\partial x} & \frac{\partial v_x}{\partial y} + \frac{\partial v_y}{\partial x} & \frac{\partial v_x}{\partial z} + \frac{\partial v_z}{\partial x} \\ \frac{\partial v_y}{\partial x} + \frac{\partial v_x}{\partial y} & 2\frac{\partial v_y}{\partial y} & \frac{\partial v_y}{\partial z} + \frac{\partial v_z}{\partial y} \\ \frac{\partial v_z}{\partial x} + \frac{\partial v_x}{\partial z} & \frac{\partial v_z}{\partial y} + \frac{\partial v_y}{\partial z} & 2\frac{\partial v_z}{\partial z} \end{bmatrix} \cdot \vec{n} \tag{6}$$

where the velocity vector is decomposed as $\vec{v} = (v_x, v_y, v_z)^{\mathrm{t}}$ in a Cartesian frame.

According to (5)-(6), the WSS vector for each of the N_{s} segmentation points of the vessel wall can be deduced from the analytical derivatives of $\vec{v}(\vec{p}; \hat{\boldsymbol{\gamma}})$ (and at each time of interest of the cardiac cycle).

At this stage, each WSS vector is expressed in its own local coordinate system $\mathcal{L}$. It must be converted to the common coordinate system for further processing.

2.5. *Step 4: Robust Post-processing*

Steps 1 to 3 allow us to estimate the WSS vector at a given POI, but also at every point in its close neighborhood (see Figure 1(c)). Thus, if we repeat these steps for several neighboring POI, we get different WSS values at the same point of the vessel wall, by considering intersecting ROIs (see Figure 1(d)). We can take profit from such redundant values to improve the WSS estimation quality, in particular in terms of robustness with respect to modeling errors in the case of complex blood flows. Let us define a robust WSS estimator $\vec{\tau}_m$ deduced from the evaluations $\vec{\tau}_j$ at n_R closest neighbors:

$$\vec{\tau}_m = \underset{\vec{\tau} \in \mathbb{R}^3}{\arg\min} \sum_{j=1}^{n_R} \Phi(\|\vec{\tau} - \vec{\tau}_j\|) \tag{7}$$

where Φ is the Huber norm [28] applied to the velocity norm:

$$\Phi(x) = \begin{cases} \varepsilon\,(|x| - \varepsilon/2) & \text{if } x > \varepsilon \\ x^2/2 & \text{otherwise} \end{cases}$$

with ε set to 10^{-3}. The computation of (7) is performed using the method of Iterative Reweighted Least-Squares (IRLS) [28].

3. Simulation Based Validation

The proposed WSS estimation method PaLMA has been thoroughly validated using simulations of 4D Flow MRI data. In Subsection 3.1, we first describe the two types of simulated blood flows that we have used as a *ground truth*. Then, we explain our method to generate MRI pseudo-data in Subsection 3.2. Finally, we define performance indices to measure the estimation error in a statistically valid way (Subsection 3.3).

3.1. *Fluid Simulation*

Two types of synthetic data are considered: analytic fluid simulation on simple geometry and CFD simulation on complex geometries.

3.1.1. *Womersley Simulation*

Womersley *et al.* [29] introduced an analytical model that deals with incompressible and viscous fluids and a pulsatile laminar flow, within a straight cylindrical tube. Womersley flow provides a unidirectional velocity-vector field aligned with the tube axis, which is valid for the whole tube at a given time.

Several existing works on WSS quantification such as [5, 13] validated their contribution on Womersley flow. Here, we also propose to check PaLMA results on it, as a preliminary test. We used the blood flow depicted in [30, Fig. 11] as a realistic input. The flow is laminar with a dynamic viscosity of 0.025 Pa.s, a Reynolds number of 700 and a Womersley number of 5.16. The tube diameter is fixed to 2 cm to simulate a non-pathological artery case. The RR time interval is set to one second. The number of components used to approximate Womersley analytical solution is set to ten times the number of cardiac phases, *i.e.*, 300 components for 30 cardiac phases. The angle between the tube axis and the grid is 23°. The resulting pulsative velocity is represented in Figure 2.

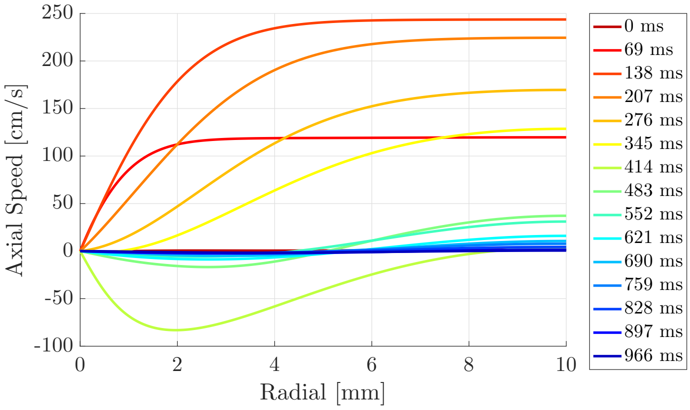

Figure 2: Axial velocity as a function of the radial position for fifteen equally spaced times of the cardiac cycle, *i.e.*, one out of two simulated phases.

3.1.2. CFD Simulation

In order to assess PaLMA performance on complex flows, we used patient-specific CFD simulations generated by Monica Sigovan and Loïc Boussel at CREATIS[3] (Lyon, France). They were computed on ANSYS Fluent with an unsteady laminar solver and considering an imposed flow rate on the inlet and a pressure drop on the outlet. The dynamic viscosity is set to 0.0035 Pa.s, leading to a Reynolds number between 110 and 480 for the four carotids. Each simulation provides the fluid velocity over a tetrahedral mesh along with the numerical evaluation of the WSS on each vessel wall point. The fluid velocity and WSS are considered as ground truth. Furthermore, the vessel wall points are assumed to be the true segmentation.

As depicted in Figure 3, we considered four carotids with different levels of stenosis. In Figure 3, each stenosis and the local area surrouding it are enclosed in a red box. None of Carotids #1 and #2 present backflow patterns, although Carotid #2 has a more severe stenosis. Carotids #3 and #4 velocity patterns correspond to the most complex ones. More specifically, Carotid #4 presents a significant backflow associated with a stenosis output jet.

3.2. Synthetic MRI Simulation

The analytical and numerical flows, described in Section 3.1, have been used to create *in silico* 4D Flow MRI datasets. To simulate the conditions of 4D Flow MRI acquisition, one can work in the k-space [17] by filtering the transversal magnetization [31, 32]. It is also possible to directly filter the velocity map, either by a Gaussian PSF [12, 3], or by mean filtering [20, 33]. Here, we adopt the mean filtering strategy. Specifically, each voxel is divided into $N_{\text{sv}} = 6 \times 6 \times 6$ sub-voxels, and the discretized PSF is constant over the N_{sv} subvoxels, so the simulated noiseless velocity is the average value among them.

The simulation on Womersley flow is performed over a 4D grid with a spatial resolution of 2.5 mm ISO and a time resolution of 34 ms. The simulated 4D grid size is 32×32×32×30. The spatial resolution on carotids is set to 1 mm ISO to simulate clinical protocols, in conformity

---

[3] https://www.creatis.insa-lyon.fr/site7/en

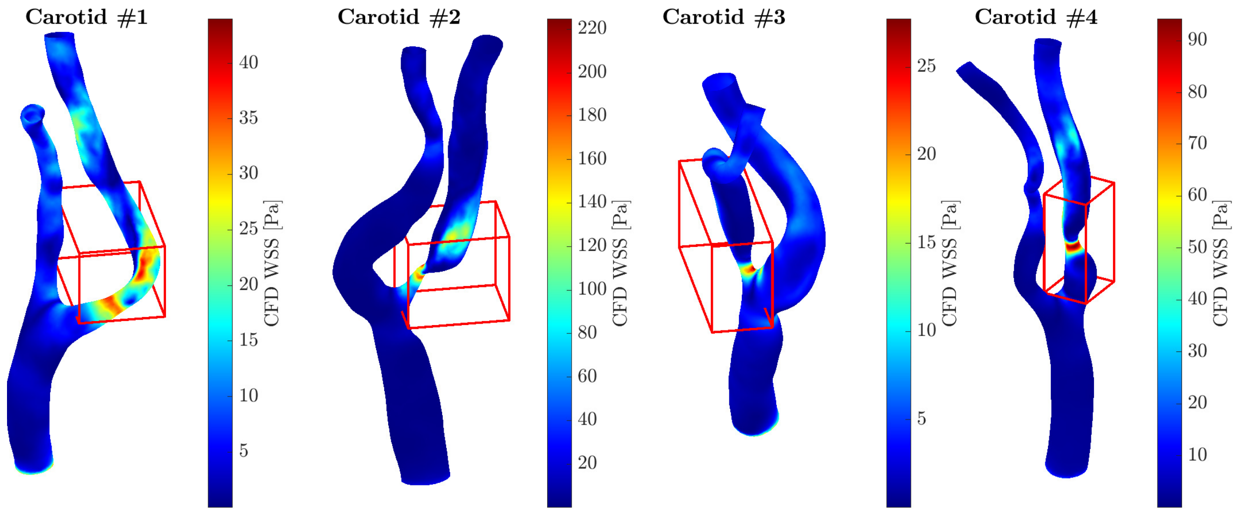

Figure 3: WSS magnitude obtained by CFD simulation over four carotid geometries at systolic time. The red boxes define local areas of interest from the clinical viewpoint.

with [14, Tab. 1]. On the other hand, Potters *et al.* [17] suggested to work at a resolution of 0.7 mm ISO to get a better WSS quantification. Consequently, we simulated both resolutions on each carotid. Each carotid are simulated with sixteen cardiac phases, uniformly distributed, with a temporal resolution between 53.5 and 62.5 ms.

Finally, we consider an additive centered Gaussian noise such that the standard deviation σ_v is equal to $\frac{\sqrt{2}}{\pi}\mathrm{Venc}/\mathrm{SNR}$ [34]. The velocity encoding is set to 120 % of the maximum velocity value.

3.3. WSS Performance Indicators

Three performance indicators have been evaluated in a systematic way. The first two directly evaluate the mismatch between the estimated WSS and the true one. Let us define the WSS Signal-to-Error Ratio (SER):

$$\mathrm{SER}(\mathrm{dB}) = 10 \times \log_{10}\left(\frac{\sum\limits_{j=1}^{N} \|\vec{\tau}_j^*\|^2}{\sum\limits_{j=1}^{N} \|\vec{\tau}_j - \vec{\tau}_j^*\|^2}\right) \tag{8}$$

where $\vec{\tau}_j^*$ is the true WSS vector, the SER being possibly averaged in space and/or time from N samples. Whereas such a performance index accounts for the fact that the WSS is a space vector, many studies [1, 35] focused their analysis on the magnitude of the WSS at the systolic peak. As a consequence, let us also define another SER index, restricted to the WSS magnitude:

$$\mathrm{SER}^{\mathrm{m}}(\mathrm{dB}) = 10 \times \log_{10}\left(\frac{\sum\limits_{j=1}^{N} \|\vec{\tau}_j^*\|^2}{\sum\limits_{j=1}^{N} \left(\|\vec{\tau}_j\| - \|\vec{\tau}_j^*\|^2\right)}\right) \tag{9}$$

Let us remark that SER is intrinsically smaller than SER^{m}, because SER also gives account of orientation errors.

Finally, we have also quantified the Pearson's correlation value r between the magnitude of the estimated WSS and the true one:

$$r = \left(\sum_{j=1}^{N} \nu_j \nu_j^* \right) \left(\sum_{j=1}^{N} \nu_j^2 \sum_{j=1}^{N} \left(\nu_j^* \right)^2 \right)^{-1/2}$$

where ν_j and ν_j^* are statistically centered WSS magnitudes:

$$\nu_j = \|\vec{\tau}_j\| - \frac{1}{N} \sum_{j=1}^{N} \|\vec{\tau}_j\|, \quad \nu_j^* = \|\vec{\tau}_j^*\| - \frac{1}{N} \sum_{j=1}^{N} \|\vec{\tau}_j^*\|.$$

Whereas SER^{m} directly measures the amount of error between $\|\vec{\tau}_j\|$ and the reference $\|\vec{\tau}_j^*\|$, the correlation coefficient r is neither sensitive to the bias nor to a possibly wrong scale of the estimated WSS. In this sense, r can be viewed as a more qualitative performance index compared to SER^{m}, which is truly quantitative.

4. Results

In this section, we evaluate the performance of WSS estimation using PaLMA, and we compare them to that of the Smoothing B-spline (SBS) method proposed by [17]. The latter being a widespread WSS evaluation technique (*e.g.,* [20, 21, 35]), entering the same local design category as PaLMA, we have found meaningful to take SBS as a reference method.

4.1. Quantification Analysis

4.1.1. Womersley Flow

Here, a fixed amount of noise is applied directly to the filtered velocity field, with an SNR of 20 dB corresponding to a noise standard deviation σ of 4.5 % of the Venc. According to [15, Fig. 5], such a regime can be considered as the worst case encountered in 4D Flow MRI at 1.5 Tesla, at the clinical routine resolution and without contrast enhancement.

Figure 4 presents the time course of the spatial mean of the z-component of the WSS. The displayed confidence intervals at 95 % are deduced from the fact that the true WSS value is constant over the 1504 considered vertices.

Figure 4 allows us to compare PaLMA to SBS, the former being also tested without accounting for the presence of the MRI filter effect. The difference between the two versions of PaLMA is noticeable, which shows the favorable impact of accounting for a more precise data model. In the rest of the paper, the presence of the MRI filter is always taken into account for PaLMA.

Figure 4 clearly shows that the output of PaLMA is significantly closer to the true WSS value than that of SBS, at nearly all phases of the cardiac cycle. In particular, SBS strongly underestimates the WSS level at all instants outside the diastole phase, where the WSS level is very low. There is also a tendency to underestimate the WSS value for PaLMA, but at a considerably reduced level. In particular, the range of the difference between the output of PaLMA and the true WSS

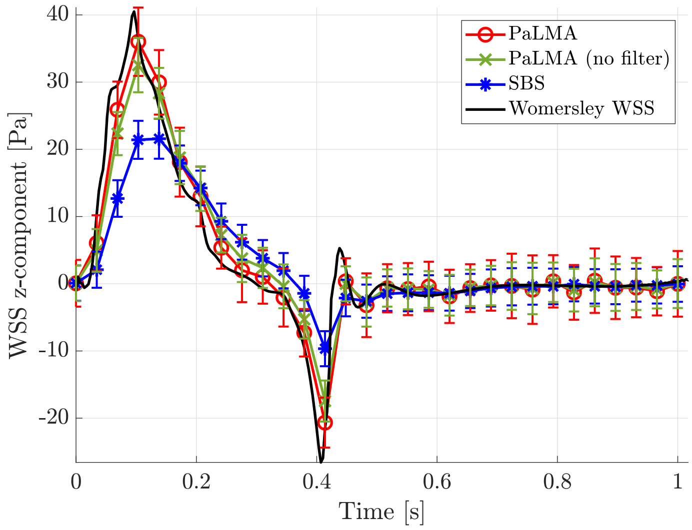

Figure 4: WSS z-component over time. For both PaLMA and SBS estimation, a 95 % confidence interval is also represented.

values is comparable to the size of the confidence interval at 95 %, which is far from being fulfilled by SBS. The diastole phase is the only time period where SBS can be considered as slightly better than PaLMA, because the variance of the latter is about 125 % of that of SBS.

In terms of performance indices, we obtain respectively SER and SER$^{\mathrm{m}}$ values of 10.5 and 12.1 dB for PaLMA, while SBS reaches 5.8 and 6.2 dB. The correlation index r is 96.7 and 85.1 % for PaLMA and SBS, respectively. The ratio between the latter two values is somewhat reduced by the fact that the correlation index does not account for the fact that SBS strongly underestimates the WSS. Nonetheless, the output of PaLMA reaches a very high correlation level, which allows us to conclude that this first validation test is undoubtedly favorable to PaLMA.

4.1.2. Carotid Flows

We now assess the performance of PaLMA and SBS on more realistic blood flows and vessel geometries. The performance indices can be evaluated over either the complete carotids (global area), or on local areas of higher interest, *i.e.*, regions in red boxes in Figure 3.

Figure 5 presents Bland-Altman plots generated from noiseless datasets. The agreement between estimated WSS magnitude and true value is analyzed for PaLMA and SBS separately. Moreover, we have found that the readability was better after log-transformation.

The systematic tendency to underestimate the WSS is confirmed for both methods, the bias being significantly stronger for SBS. In all cases, the points clouds obtained for PaLMA are more elongated and flattened, whereas those obtained for SBS have a negative slope of larger magnitude.

Table 2 gathers all performance indices on noisy datasets with an SNR of 20 dB, computed either globally or locally, and either at all cardiac phases ($\forall t$), or at systolic times t_{s} only. PaLMA significantly improves all the indices. In terms of SER and of SER$^{\mathrm{m}}$, the gain is respectively of 1.4 to 3.8 dB and 1.9 to 5.8 dB for global and local estimation, respectively. Besides, let us note that the correlation levels obtained for SBS within our simulations confirm the range reported in [21], while PaLMA systematically improves this performance index from 0.2 to 21.7 %.

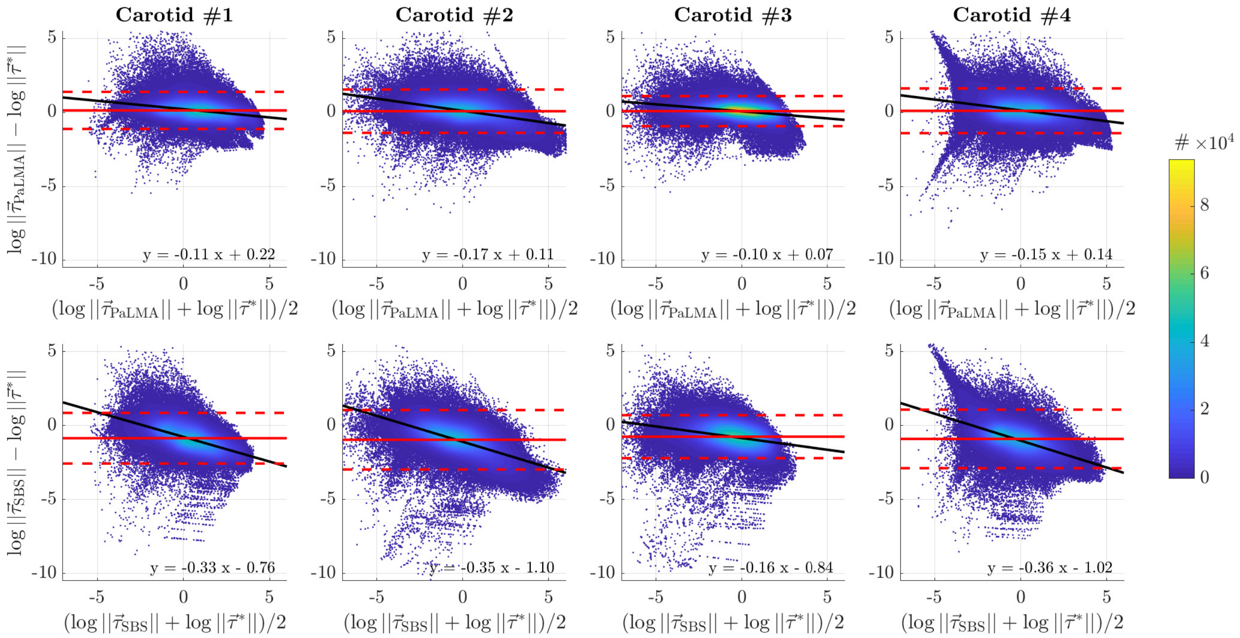

Figure 5: Bland-Altman diagrams of WSS estimation using PaLMA and SBS after logarithmic transformation for each carotid. Global areas are considered, at all phases of the cardiac cycle. The color of the points indicates the local density of the cloud, with a scale given by the colorbar on the right. The regression line is shown in black. The mean and the 95 % confidence interval are respectively depicted by the solid and dashed horizontal red lines.

Carotid #	1				2				3				4			
Area	global		local		global		local		global		local		global		local	
Time	$\forall t$	t_s	$\forall t$	t_s	$\forall t$	t_s	$\forall t$	t_s	$\forall t$	t_s	$\forall t$	t_s	$\forall t$	t_s	$\forall t$	t_s
Method	**PaLMA**															
SER [dB]	**5.8**	**5.8**	**5.9**	**5.6**	**2.8**	**2.9**	**2.8**	**2.5**	**5.5**	**5.7**	**3.4**	**3.4**	**3.7**	**4.2**	**4.2**	**4.1**
SER$^{\mathrm{m}}$ [dB]	**7.8**	**7.7**	**8.4**	**8**	**3.4**	**3.3**	**3.2**	**2.9**	**6.5**	**6.7**	**4.1**	**4.1**	**4.9**	**5**	**4.6**	**4.4**
r [%]	**86.4**	**82.6**	**89.8**	**73.6**	**79.3**	**82**	**83.5**	**81.7**	**78.9**	**69.9**	**77.6**	**72.1**	**78**	**76.8**	**80.4**	**76.8**
Method	**SBS**															
SER [dB]	2.5	2.3	2.1	1.8	0.9	0.9	0.8	0.7	3.2	3.1	2	1.9	1.8	1.6	1.6	1.4
SER$^{\mathrm{m}}$ [dB]	3	2.6	2.6	2.2	1.1	1	0.9	0.8	3.7	3.6	2.2	2.2	2	1.8	1.7	1.5
r [%]	79.7	75	84.5	64.2	57.6	67.1	70.1	68	73.1	61.3	71.6	65.9	71.9	72.1	78.4	76.6

Table 2: Performance indices SER, SER$^{\mathrm{m}}$, and r for PaLMA and SBS [17] applied to the four carotid simulations with a SNR of 20 dB. The considered area is either global, *i.e.*, the whole carotid wall, or it is otherwise limited to local areas of interest (*cf.* Figure 3) for all cardiac phases ($\forall t$) or at systolic times t_s only. The presented results are averaged over 20 noise realizations.

For both methods, the performance indices depend on several parameters such as the maximum WSS level, and the complexity of the vessel wall geometry and of the fluid pattern. Carotid #1 corresponds to the most favorable case, the fluid pattern being the simplest. Carotid #2 induces more complex datasets, because it displays a severe stenosis that generates higher WSS levels. Moreover, let us stress that high-velocity jets call for larger Venc values, which deteriorates the

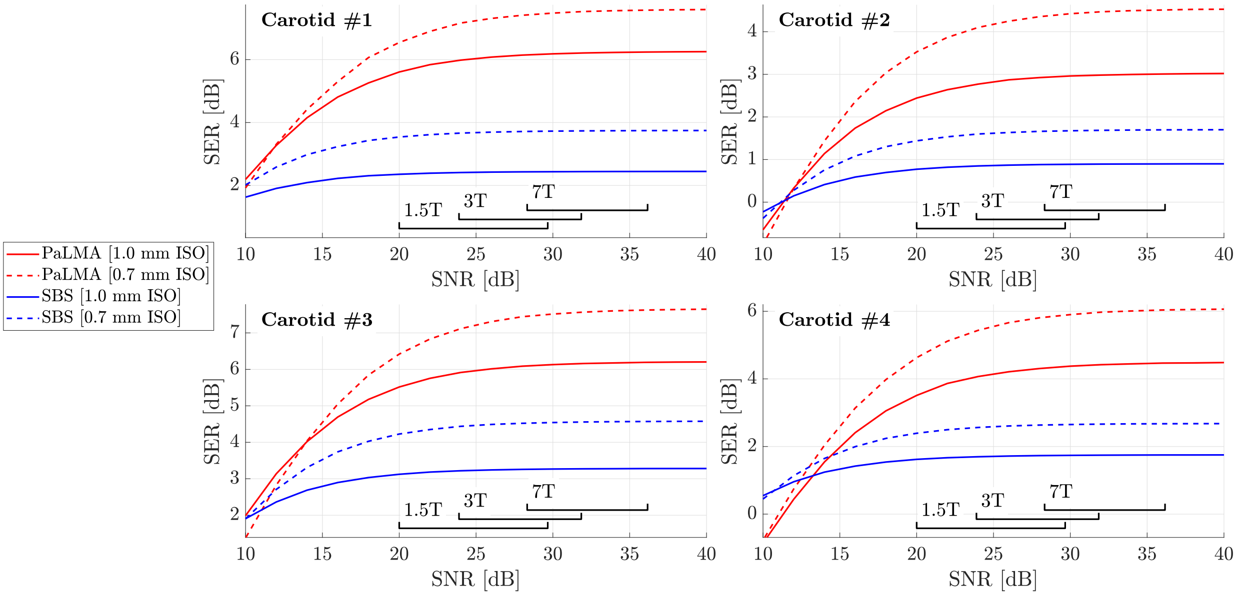

Figure 6: Performance of PaLMA and SBS in terms of SER as a function of the SNR for the four carotids. Typical SNR intervals obtained in 4D Flow are reported depending on the magnetic field strength [15]. The presented results are averaged over 20 noise realizations.

SNR in areas and at cardiac phases of lower velocity.

Finally, we can observe that the quantification error is the largest in the internal and external carotid arteries, where the diameter is reduced to four to five voxels only (against nine to ten voxels in the common carotid artery). This observation matches an observation from [17], that at least eight voxels are necessary to obtain a 5 % accuracy. Furthermore, observations on vessel wall points with complex flows in their vicinity lead us to conclude that a significant part of the error is due to the coarse resolution of the data. In particular, some back-flow effects are likely to appear at scales that are too small to be detectable from the MRI data at a resolution of 1 mm ISO.

4.2. Sensitivity to SNR and Resolution

Here, we test the WSS estimation methods in different situations in terms of SNR and of spatial resolution of the 4D Flow MRI data.

In thoracic 4D Flow MRI, the SNR varies between 20 and 36 dB [15], depending on the magnetic field strength, the resolution for a specific Field Of View (FOV), the acceleration factor in parallel imaging and the contrast agent usage. In this work, we assume that the SNR range is similar for intracranial acquisitions. We have considered a wide range of SNR values from 10 to 40 dB to evaluate the robustness of both PaLMA and SBS methods. Several contributions rather evaluate the amount of noise in terms of standard deviation relative to the Venc [17, 2, 3]. Typically, 5 to 10 % of the Venc are considered. For sake of comparison, SNR levels of 10, 20, and 40 dB correspond to 14.2, 4.5, and 0.45 % of the Venc.

We have also tested the difference in terms of WSS estimation between a spatial resolution of 1 mm ISO, which corresponds to clinical standards in 4D Flow MRI [14], and an improved resolution of 0.7 mm ISO, as suggested in [17].

Figure 6 displays the SER as a function of the SNR for each carotid and considering both resolutions. The SER value is averaged over all the vessel wall points and at all cardiac phases. For each graph, typical SNR intervals are indicated, corresponding to different magnetic field strengths for both contrast modalities (with and without contrast enhancement) [15].

At the resolution of 1 mm, PaLMA presents a gain of 1.6 to 3.2 dB compared to SBS, which is almost constant within SNR intervals typical of 4D Flow MRI. We can draw the same conclusion for the higher resolution of 0.7 mm ISO, with the important observation that the gain is significantly larger, from 2 to 2.9 dB. Moreover, the improvement is higher for Carotid #2, which is the most severe case of stenosis. It is only at very low SNR values (less than 14 dB, *i.e.*, a standard deviation of more than 9 % of the Venc) that SBS performs better than PaLMA. We make the assumption that the performance of SBS benefits from its relatively simpler and more strongly regularized structure compared to PaLMA, in such situations. As mentioned earlier, regularized methods are subject to the risk of oversmoothing the WSS. These graphs illustrate that the level of regularization of PaLMA represents an appropriate tradeoff for 4D Flow MRI applications.

Pearson correlation evolves similarly to the SER. It reaches a plateau for an SNR around 25 dB. Table 3 gathers Pearson's correlation intervals, obtained by averaging the performance over all vessel wall points and all cardiac phases, for SNR values from 20 to 36 dB. Once again, one can observe a significant improvement due to a finer resolution of 0.7 mm ISO. Moreover, the performance of PaLMA is uniformly better than that of SBS.

Method	**PaLMA**		**SBS**	
Resolution (mm ISO)	0.7	1	0.7	1
#1	**90-91.9**	**86.5-87.8**	83-86.5	78.4-82.9
#2	**84.5-89.3**	**77-83.3**	69.5-82.3	52.5-72.9
#3	**83.5-86.6**	**78-81.2**	74.5-79.1	71-75.6
#4	**84.5-88.8**	**76.7-82.2**	74.5-81.4	69-77.9

Table 3: Pearson correlation r [%] for a SNR range of 20 to 36 dB and for the four Carotids #1 to #4.

Let us mention that we have performed additional performance comparisons focused at local areas (*cf.* Figure 3), or at systolic time. At average SNR values of at least 20 dB, we obtain the same general conclusions as the previous ones, based on global averaging. Moreover, for lower SNR between 10 to 20 dB, we observe that PaLMA remains superior to SBS, because the velocity-to-noise ratio is more favorable in the stenosis area and at systolic time.

Finally, unless more efficient MRI sequences become available, MRI data acquisition at a finer resolution generally comes with a loss in terms of SNR level. Based on the SNR model of [36], an SNR loss of 14 dB is a price to pay for choosing a finer resolution of 0.7 mm ISO instead of the clinical routine resolution of 1.0 mm ISO. At sufficiently high SNR levels (typically, for SNR levels of 24 dB at least), we conclude that data acquisition at 0.7 mm ISO could be a better choice to evaluate the WSS at systolic time, for instance. Let us notice that a clinical SNR of 24 dB is reachable on a 1.5T MRI thanks to contrast enhancement, or with 3T MRI acquisitions [15].

5. Conclusion and Discussion

We have proposed a new method of WSS quantification from 4D Flow MRI data, called Parametric Local Morphology Algorithm (PaLMA). It relies on a parametric description of the vessel wall and of the blood velocity field in the vicinity of each point of interest. Because PaLMA is based on spatial models at the local scale, it bypasses any complex 3D processing step, such as volumic mesh generation [2], or 3D interpolation [20].

Extensive validations have been performed on simulated datasets. We have exploited blood flows simulated by CFD from segmented carotids as realistic case of blood velocities. We have also considered realistic parameter values in the context of cardiovascular medical imaging, regarding the spatial resolution of MRI data, the partial volume effect, and the signal to noise ratio. More specifically, we have considered noise levels that incorporate background phase corrections, according to [15]. As a perspective, the effect of additional artefacts could be tested also, such as eddy-current and Maxwell terms effects, magnetic field inhomogeneity, imperfect segmentations of the vessel wall, and Venc aliasing. This could be the topic of a future *in-vitro* or *in-vivo* study.

In the tested conditions, PaLMA performs significantly better than the smoothing B-spline method proposed by Potters *et al.* in [17], considered here as a reference method, both in terms of correlation with the true WSS value, and of absolute error norm. In particular, both methods tend to underestimate the WSS value, but PaLMA provides a strong reduction of the mismatch. We attribute the overall improvement brought by PaLMA in terms of WSS quantification accuracy to two elements.

On the first hand, PaLMA relies on a spatial filter model to relate the 4D MRI data to the underlying velocity field. This allows us to manage the partial volume effect in a satisfying manner, the impact of the latter being significant near the vessel wall.

On the other hand, PaLMA consistently exploits the available data around the point of interest using a spatial model of both the wall surface and the velocity field. In comparison, Potters *et al.*'s method relies on two interpolation steps, the second one being one-dimensional, a WSS value being finally deduced from the interpolated velocity at only three aligned points. Potters *et al.*'s procedure brings robustness at very low SNR levels, but it limits the estimation quality in realistic acquisition conditions. Given the constant progress in the domain of acquisition sequences, PaLMA thus appears as a better choice than Potters *et al.*'s method to fully benefit from improved acquisition conditions.

The fact that PaLMA relies on spatial models does not mean that it is computationally more costly that Potters *et al.*'s method, since we have limited ourselves to simple polynomial models. In practice, the computing time is equivalent for both methods. With parallel computation, it is between 5 and 7 minutes for one carotid over the full cardiac cycle, with an eight thread CPU system (Intel Core i7-6820HQ, 2.70 GHz) equipped with 32GB RAM.

Several possible improvements of PaLMA can be envisaged. One could consist in exploiting a fluid incompressibility constraint, *i.e.*, to impose a zero divergence condition to the blood velocity model, with the hope to get a more precise or a more robust WSS value. Another possibility would be to explore the possibilities of spatio-temporal models of blood velocity, while the present version of PaLMA separately process the MRI data at different phases of the cardiac cycle. However, a prerequisite to rely on a temporal model of the blood velocity field is that a precise volume registration must be performed between successive frames of the cardiac cycle.

Acknowledgement

We would like to thank Monica Sigovan and Loïc Boussel from CREATIS (Lyon, France) for generously letting us rely on their patient-specific computational fluid dynamic simulations for our performance study. Our thanks also go to Wouter V. Potters for kindly sharing the source code of the smoothing B-spline method proposed in [17]. This work is supported by a grant from the Region Pays de la Loire, under the regional scientific challenge project MRI-Quantif.

Appendix A. Vessel Surface Fitting

For each POI, let $\vec{p}_1, \ldots, \vec{p}_{n_R}$ stand for the positions of the n_R vertices in the local system $\mathcal{L}$, with $\vec{p}_n = [x_n, y_n, z_n]^{\mathrm{t}}$. On the other hand, let us introduce the vector-valued function

$$\boldsymbol{m}(x,y) = \left[x, y, xy, x^2, y^2, yx^2, xy^2, x^3, y^3\right]^{\mathrm{t}},$$

so that the cubic equation (1) also reads $z = \boldsymbol{m}(x,y)^{\mathrm{t}}\boldsymbol{\theta}$. Then, the LS criterion to be minimized can be expressed as

$$\sum_{n=1}^{n_R} \left(z_n - \boldsymbol{m}(x_n, y_n)^{\mathrm{t}}\boldsymbol{\theta}\right)^2 = \|\boldsymbol{z} - \boldsymbol{M}\boldsymbol{\theta}\|^2,$$

where

$$\boldsymbol{z} = [z_1, \ldots, z_{n_R}]^{\mathrm{t}}, \qquad \boldsymbol{M} = [\boldsymbol{m}(x_1, y_1), \ldots, \boldsymbol{m}(x_{n_R}, y_{n_R})]^{\mathrm{t}}.$$

The LS solution is then given by $\boldsymbol{\theta} = (\boldsymbol{M}^{\mathrm{t}}\boldsymbol{M})^{-1}\boldsymbol{M}^{\mathrm{t}}\boldsymbol{z}$, provided that $\boldsymbol{M}$ is an invertible matrix, a necessary condition being that n_R is not smaller than nine.

Appendix B. Velocity Model Fitting

The spatial convolution $h \star \vec{v}$ is defined as

$$(h \star \vec{v})(x,y,z) = \iiint h(x', y', z')\, \vec{v}(x - x', y - y', z - z')\, dx'\, dy'\, dz', \tag{B.1}$$

In practice, we have implemented a discrete approximation of (B.1) on regular subgrids with a finer resolution than the MRI acquisition grid, each voxel being divided into subvoxels, so that

$$(h \star \vec{v})(\vec{p}_i) \approx \sum_{j',k',\ell'} h_{j',k',\ell'} \vec{v}(x_{j-j'}, y_{k-k'}, z_{\ell-\ell'}), \tag{B.2}$$

where $\vec{p}_i = (x_j, y_k, z_\ell)$ corresponds to a position of an MRI data point in the ROI, while the right-hand-side summation is over a finer subgrid of N_{sv} subvoxels centered around $\vec{p}_{j,k,\ell}$. For each velocity component, Eq. (B.2) can be compactly written as a scalar product, such as $(h \star v_x)(\vec{p}_i) \approx \boldsymbol{h}^{\mathrm{t}}\boldsymbol{v}_{x,i}$ for the x component, where $\boldsymbol{h}$ is the discretized PSF (stacked as a column vector), and $\boldsymbol{v}_{x,i}$

is an N_{sv}-length vector gathering the x components of the velocity model computed on the subgrid around position $\vec{p}_i$.

In order to compute $\hat{\gamma}$ according to (4), let us first remark that the problem decomposes into separate LS subproblems, so that $\hat{\gamma} = \left(\hat{\gamma}_x, \hat{\gamma}_y, \hat{\gamma}_z\right)$, each component being computed separately. For instance, $\hat{\boldsymbol{\gamma}}_x$ minimizes the criterion

$$\sum_{i=1}^{N_R} w_i \left(u_{x,i} - \boldsymbol{h}^{\text{t}} \boldsymbol{v}_{x,i}\right)^2 , \tag{B.3}$$

with $\vec{u}_i = (u_{x,i}, u_{y,i}, u_{z,i})$. Equivalently, we have

$$\hat{\boldsymbol{\gamma}}_x = \underset{\boldsymbol{\gamma}_x \in \mathbb{R}^{N_P}}{\arg\min} \sum_{i=1}^{N_R} w_i \left(u_{x,i} - \boldsymbol{h}^{\text{t}} \boldsymbol{P}_i \boldsymbol{\gamma}_x\right)^2$$

where each row of matrix $\boldsymbol{P}_i$ encodes the linear dependance of the x component of the velocity on parameter vector $\boldsymbol{\gamma}_x$ according to (2)-(3). Finally, let $\boldsymbol{u}_x = [u_{x,1}, \ldots, u_{x,N_R}]$, $\boldsymbol{W} = \text{Diag}(w_1, \ldots, w_{N_R})$ and $\boldsymbol{Q} = \left[\boldsymbol{P}_1^{\text{t}} \boldsymbol{h}, \ldots, \boldsymbol{P}_{N_R}^{\text{t}} \boldsymbol{h}\right]^{\text{t}}$, so that

$$\hat{\boldsymbol{\gamma}}_x = \underset{\boldsymbol{\gamma}_x \in \mathbb{R}^{N_P}}{\arg\min} (\boldsymbol{u}_x - \boldsymbol{Q}\boldsymbol{\gamma}_x)^{\text{t}} \boldsymbol{W} (\boldsymbol{u}_x - \boldsymbol{Q}\boldsymbol{\gamma}_x) = (\boldsymbol{Q}\boldsymbol{W}\boldsymbol{Q})^{-1} \boldsymbol{Q}^{\text{t}} \boldsymbol{W} \boldsymbol{u}_x,$$

with the necessary condition $N_R \geq N_P$. In the same way, we get $\hat{\boldsymbol{\gamma}}_y = (\boldsymbol{Q}\boldsymbol{W}\boldsymbol{Q})^{-1} \boldsymbol{Q}^{\text{t}} \boldsymbol{W} \boldsymbol{u}_y$ and $\hat{\boldsymbol{\gamma}}_z = (\boldsymbol{Q}\boldsymbol{W}\boldsymbol{Q})^{-1} \boldsymbol{Q}^{\text{t}} \boldsymbol{W} \boldsymbol{u}_z$.

References

[1] L. Boussel, V. Rayz, A. Martin, G. Acevedo-Bolton, M. T. Lawton, R. Higashida, W. S. Smith, W. L. Young, D. Saloner, Phase-contrast magnetic resonance imaging measurements in intracranial aneurysms in vivo of flow patterns, velocity fields, and wall shear stress: comparison with computational fluid dynamics., Magn Reson Med 61 (2009) 409–17. doi:10.1002/mrm.21861.

[2] J. Sotelo, J. Urbina, I. Valverde, C. Tejos, P. Irarrázaval, M. E. Andia, S. Uribe, D. E. Hurtado, 3D quantification of wall shear stress and oscillatory shear index using a finite-element method in 3D CINE PC-MRI data of the thoracic aorta, IEEE Trans Med Imaging 35 (6) (2016) 1475–1487. doi:10.1109/TMI.2016.2517406.
URL `http://ieeexplore.ieee.org/document/7383317/?reload=true`

[3] F. Piatti, S. Pirola, M. Bissell, I. Nesteruk, F. Sturla, A. D. Corte, A. Redaelli, E. Votta, Towards the improved quantification of in vivo abnormal wall shear stresses in BAV-affected patients from 4D-Flow imaging: Benchmarking and application to real data, J Biomech 50 (2017) 93–101, biofluid mechanics of multitude pathways: From cellular to organ. doi:https://doi.org/10.1016/j.jbiomech.2016.11.044.
URL `http://www.sciencedirect.com/science/article/pii/S0021929016312234`

[4] A. M. Malek, S. L. Alper, S. Izumo, Hemodynamic shear stress and its role in atherosclerosis, JAMA 282 (21) (1999) 2035–2042. arXiv:/data/journals/jama/4714/jsc90181.pdf, doi:10.1001/jama.282.21.2035.
URL + `http://dx.doi.org/10.1001/jama.282.21.2035`

[5] A. J. Barker, C. Lanning, R. Shandas, Quantification of hemodynamic wall shear stress in patients with bicuspid aortic valve using Phase-Contrast MRI, Ann Biomed Eng 38 (3) (2010) 788–800. doi:10.1007/s10439-009-9854-3.
URL `https://doi.org/10.1007/s10439-009-9854-3`

[6] M. E. McCormick, E. Manduchi, W. R. Witschey, R. C. Gorman, J. H. Gorman, Y.-Z. Jiang, C. J. Stoeckert, A. J. Barker, S. Yoon, M. Markl, P. F. Davies, Spatial phenotyping of the endocardial endothelium as a function of intracardiac hemodynamic shear stress, J Biomech 50 (2017) 11 – 19, biofluid mechanics of multitude pathways: From cellular to organ. doi:https://doi.org/10.1016/j.jbiomech.2016.11.018.
URL `http://www.sciencedirect.com/science/article/pii/S0021929016311861`

[7] P. van Ooij, W. V. Potters, J. Collins, M. Carr, J. Carr, S. C. Malaisrie, P. W. M. Fedak, P. M. McCarthy, M. Markl, A. J. Barker, Characterization of abnormal wall shear stress using 4D Flow MRI in human bicuspid aortopathy, Ann Biomed Eng 43 (6) (2015) 1385–1397. doi:10.1007/s10439-014-1092-7.
URL `https://doi.org/10.1007/s10439-014-1092-7`

[8] J. Sotelo, L. Dux-Santoy, A. Guala, J. Rodríguez?Palomares, A. Evangelista, C. Sing-Long, J. Urbina, J. Mura, D. E. Hurtado, S. Uribe, 3D axial and circumferential wall shear stress from 4D flow MRI data using a finite element method and a laplacian approach, Magn Reson Med 79 (5) (2017) 2816–2823. arXiv:https://onlinelibrary.wiley.com/doi/pdf/10.1002/mrm.26927, doi:10.1002/mrm.26927.
URL `https://onlinelibrary.wiley.com/doi/abs/10.1002/mrm.26927`

[9] A. Harloff, S. Berg, A. J. Barker, J. Schöllhorn, M. Schumacher, C. Weiller, M. Markl, Wall shear stress distribution at the carotid bifurcation: influence of eversion carotid endarterectomy, Eur Radiol 23 (12) (2013) 3361–3369. doi:10.1007/s00330-013-2953-4.
URL `https://doi.org/10.1007/s00330-013-2953-4`

[10] M. Cibis, W. V. Potters, F. Gijsen, H. Marquering, P. Ooij, E. Vanbavel, J. Wentzel, A. J. Nederveen, The effect of spatial and temporal resolution of cine phase contrast MRI on wall shear stress and oscillatory shear index assessment, PLoS ONE 11 (2016) e0163316. doi:10.1371/journal.pone.0163316.

[11] S. Oyre, S. Ringgaard, S. Kozerke, W. P. Paaske, M. B. Scheidegger, P. Boesiger, E. M. Pedersen, Quantitation of circumferential subpixel vessel wall position and wall shear stress by multiple sectored three-dimensional paraboloid modeling of velocity encoded cine MR, Magn Reson Med 40 (5) (1998) 645–655. arXiv:https://onlinelibrary.wiley.com/doi/pdf/10.1002/mrm.1910400502, doi:10.1002/mrm.1910400502.
URL `https://onlinelibrary.wiley.com/doi/abs/10.1002/mrm.1910400502`

[12] A. Stalder, M. Russe, A. Frydrychowicz, J. Bock, J. Hennig, M. Markl, Quantitative 2D and 3D phase contrast MRI: Optimized analysis of blood flow and vessel wall parameters, Magn Reson Med 60 (5) (2008) 1218–1231. doi:10.1002/mrm.21778.
URL `http://dx.doi.org/10.1002/mrm.21778`

[13] J. Sotelo, J. Urbina, I. Valverde, C. Tejos, P. Irarrázaval, D. E. Hurtado, S. Uribe, Quantification of wall shear stress using a finite-element method in multidimensional phase-contrast MR data of the thoracic aorta, J Biomech 48 (10) (2015) 1817 – 1827. doi:https://doi.org/10.1016/j.jbiomech.2015.04.038.
URL `http://www.sciencedirect.com/science/article/pii/S0021929015002584`

[14] M. Markl, A. Frydrychowicz, S. Kozerke, M. Hope, O. Wieben, 4D Flow MRI, J Magn Reson Imaging 36 (5) (2012) 1015–1036. doi:10.1002/jmri.23556.
URL `http://dx.doi.org/10.1002/jmri.23556`

[15] A. T. Hess, M. M. Bissell, N. A. Ntusi, A. J. Lewis, E. M. Tunnicliffe, A. Greiser, A. F. Stalder, J. M. Francis, S. G. Myerson, S. Neubauer, M. D. Robson, Aortic 4D flow: Quantification of signal-to-noise ratio as a function of field strength and contrast enhancement for 1.5T, 3T, and 7T, Magn Reson Med 73 (5) (2015) 1864–1871. arXiv:https://onlinelibrary.wiley.com/doi/pdf/10.1002/mrm.25317, doi:10.1002/mrm.25317.
URL `https://onlinelibrary.wiley.com/doi/abs/10.1002/mrm.25317`

[16] U. Köhler, I. Marshall, M. B. Robertson, Q. Long, X. Y. Xu, P. R. Hoskins, MRI measurement of wall shear stress vectors in bifurcation models and comparison with CFD predictions, J Magn Reson Imaging 14 (5) (2001) 563–573. arXiv:https://onlinelibrary.wiley.com/doi/pdf/10.1002/jmri.1220, doi:10.1002/jmri.1220.
URL `https://onlinelibrary.wiley.com/doi/abs/10.1002/jmri.1220`

[17] W. V. Potters, P. Ooij, H. Marquering, E. vanBavel, A. J. Nederveen, Volumetric arterial wall shear stress calculation based on cine phase contrast MRI, J Magn Reson Imaging 41 (2) (2015) 505–516. arXiv:https://onlinelibrary.wiley.com/doi/pdf/10.1002/jmri.24560, doi:10.1002/jmri.24560.
URL `https://onlinelibrary.wiley.com/doi/abs/10.1002/jmri.24560`

[18] E. M. Masutani, F. Contijoch, E. Kyubwa, J. Cheng, M. T. Alley, S. Vasanawala, A. Hsiao, Volumet-

ric segmentation-free method for rapid visualization of vascular wall shear stress using 4D Flow MRI, Magn Reson Med 80 (2) (2018) 748–755. arXiv:https://onlinelibrary.wiley.com/doi/pdf/10.1002/mrm.27159, doi:10.1002/mrm.27159.
URL https://onlinelibrary.wiley.com/doi/abs/10.1002/mrm.27159

[19] S. Petersson, P. Dyverfeldt, T. Ebbers, Assessment of the accuracy of MRI wall shear stress estimation using numerical simulations, J Magn Reson Imaging 36 (1) (2012) 128–138. arXiv:https://onlinelibrary.wiley.com/doi/pdf/10.1002/jmri.23610, doi:10.1002/jmri.23610.
URL https://onlinelibrary.wiley.com/doi/abs/10.1002/jmri.23610

[20] M. Cibis, W. V. Potters, F. J. H. Gijsen, H. Marquering, E. vanBavel, A. F. W. van der Steen, A. J. Nederveen, J. J. Wentzel, Wall shear stress calculations based on 3D cine phase contrast MRI and computational fluid dynamics: a comparison study in healthy carotid arteries, NMR Biomed 27 (7) (2014) 826–834. arXiv:https://onlinelibrary.wiley.com/doi/pdf/10.1002/nbm.3126, doi:10.1002/nbm.3126.
URL https://onlinelibrary.wiley.com/doi/abs/10.1002/nbm.3126

[21] M. Cibis, W. V. Potters, M. Selwaness, F. J. Gijsen, O. H. Franco, A. M. A. Lorza, M. de Bruijne, A. Hofman, A. van der Lugt, A. J. Nederveen, J. J. Wentzel, Relation between wall shear stress and carotid artery wall thickening MRI versus CFD, J Biomech 49 (5) (2016) 735 – 741. doi:https://doi.org/10.1016/j.jbiomech.2016.02.004.
URL http://www.sciencedirect.com/science/article/pii/S0021929016300987

[22] J. Idier (Ed.), Bayesian Approach to Inverse Problems, ISTE Ltd and John Wiley & Sons Inc, 2008. doi:10.1002/9780470611197.

[23] M. Alexa, J. Behr, D. Cohen-Or, S. Fleishman, D. Levin, C. T. Silva, Point set surfaces, in: Proceedings of the Conference on Visualization ’01, VIS ’01, IEEE Computer Society, Washington, DC, USA, 2001, pp. 21–28.
URL http://dl.acm.org/citation.cfm?id=601671.601673

[24] D. Levin, Mesh-independent surface interpolation, in: G. Brunnett, B. Hamann, H. Müller, L. Linsen (Eds.), Geometric Modeling for Scientific Visualization, Springer Berlin Heidelberg, Berlin, Heidelberg, 2004, pp. 37–49.

[25] B. Ridel, G. Guennebaud, P. Reuter, X. Granier, Parabolic-cylindrical moving least squares surfaces, Comput Graph 51 (C) (2015) 60–66. doi:10.1016/j.cag.2015.05.006.
URL http://dx.doi.org/10.1016/j.cag.2015.05.006

[26] L. Coghlan, H. R. Singleton, L. J. Dell’Italia, C. E. Linderholm, G. M. Pohost, Measurement of three-dimensional normal vectors, principal curvatures, and wall thickness of the heart using cine-MRI, in: E. A. Hoffman (Ed.), Medical Imaging 1995: Physiology and Function from Multidimensional Images, Vol. 2433 of SPIE, 1995, pp. 292–302. doi:10.1117/12.209703.

[27] L. Zhong, Y. Su, S.-Y. Yeo, R.-S. Tan, D. N. Ghista, G. Kassab, Left ventricular regional wall curvedness and wall stress in patients with ischemic dilated cardiomyopathy, Am J Physiol-Heart C 296 (3) (2009) H573–H584, pMID: 19122166. arXiv:https://doi.org/10.1152/ajpheart.00525.2008, doi:10.1152/ajpheart.00525.2008.
URL https://doi.org/10.1152/ajpheart.00525.2008

[28] P. J. Huber, Robust Statistics, John Wiley, New York, NY, USA, 1981.

[29] J. R. Womersley, Method for the calculation of velocity, rate of flow and viscous drag in arteries when the pressure gradient is known, J Physiol 127 (3) (1955) 553–563. doi:10.1113/jphysiol.1955.sp005276.
URL http://dx.doi.org/10.1113/jphysiol.1955.sp005276

[30] C. Puelz, S. Čanić, B. Rivière, C. G. Rusin, Comparison of reduced models for blood flow using Runge-Kutta discontinuous Galerkin methods, Appl Numer Math 115 (2017) 114 – 141. doi:http://dx.doi.org/10.1016/j.apnum.2017.01.005.
URL http://www.sciencedirect.com/science/article/pii/S0168927417300077

[31] Z. Liang, P. Lauterbur, Principles of Magnetic Resonance Imaging: A Signal Processing Perspective, IEEE Press Series on Biomedical Engineering, Wiley, 1999.
URL https://books.google.fr/books?id=LzVDAQAAIAAJ

[32] A. Constantinesco, J. Mallet, A. Bonmartin, C. Lallot, A. Briguet, Spatial or flow velocity phase encoding gradients in NMR imaging, Magn Reson Imaging 2 (4) (1984) 335 – 340. doi:http://dx.doi.org/10.1016/0730-725X(84)90200-5.
URL http://www.sciencedirect.com/science/article/pii/0730725X84902005

[33] T. Puiseux, A. Sewonu, O. Meyrignac, H. Rousseau, F. Nicoud, S. Mendez, R. Moreno, Reconciling PC-MRI and CFD: An in-vitro study, NMR Biomed 32 (5) (2019) e4063, e4063 nbm.4063. arXiv:https://www.onlinelibrary.wiley.com/doi/pdf/10.1002/nbm.4063, doi:10.1002/nbm.4063.
URL `https://www.onlinelibrary.wiley.com/doi/abs/10.1002/nbm.4063`

[34] A. T. Lee, G. B. Pike, N. J. Pelc, Three-point phase-contrast velocity measurements with increased velocity-to-noise ratio, Magn Reson Med 33 (1) (1995) 122–126. doi:10.1002/mrm.1910330119.
URL `https://doi.org/10.1002/mrm.1910330119`

[35] P. van Ooij, A. L. Powell, W. V. Potters, J. C. Carr, M. Markl, A. J. Barker, Reproducibility and interobserver variability of systolic blood flow velocity and 3D wall shear stress derived from 4D Flow MRI in the healthy aorta, J Magn Reson Imaging 43 (1) (2016) 236–248. arXiv:https://onlinelibrary.wiley.com/doi/pdf/10.1002/jmri.24959, doi:10.1002/jmri.24959.
URL `https://onlinelibrary.wiley.com/doi/abs/10.1002/jmri.24959`

[36] A. Macovski, Noise in MRI, Magn Reson Med 36 (3) (1996) 494–497. arXiv:https://onlinelibrary.wiley.com/doi/pdf/10.1002/mrm.1910360327, doi:10.1002/mrm.1910360327.
URL `https://onlinelibrary.wiley.com/doi/abs/10.1002/mrm.1910360327`